Redox Biology 75 (2024) 103301

Contents lists available at ScienceDirect

Redox Biology

journal homepage: www.elsevier.com/locate/redox

TDP-43 dysfunction leads to bioenergetic failure and lipid metabolic rewiring in human cells

Miriam Ceron-Codorniu [a], Pascual Torres [a], Anna Fernàndez-Bernal [a], Santiago Rico-Rios [a], José CE. Serrano [a], Maria P. Miralles [b], Maria Beltran [b], Ana Garcera [b], Rosa M. Soler [b], Reinald Pamplona [a], Manuel Portero-Otín [a,*]

[a] Metabolic Pathophysiology Research Group, Universitat de Lleida-IRBLleida, 25198, Lleida, Spain
[b] Neuronal Signaling Unit, Universitat de Lleida-IRBLleida, 25198, Lleida, Spain

ARTICLE INFO

Keywords:
Amyotrophic lateral sclerosis
ACSL4
TDP-43
In vitro models
Homeostasis

ABSTRACT

The dysfunction of TAR DNA-binding protein 43 (TDP-43) is implicated in various neurodegenerative diseases, though the specific contributions of its toxic gain-of-function versus loss-of-function effects remain unclear. This study investigates the impact of *TARDBP* loss on cellular metabolism and viability using human-induced pluripotent stem cell-derived motor neurons and HeLa cells. *TARDBP* silencing led to reduced metabolic activity and cell growth, accompanied by neurite degeneration and decreased oxygen consumption rates in both cell types. Notably, *TARDBP* depletion induced a metabolic shift, impairing ATP production, increasing metabolic inflexibility, and elevating free radical production, indicating a critical role for TDP-43 in maintaining cellular bioenergetics. Furthermore, *TARDBP* loss triggered non-apoptotic cell death, increased ACSL4 expression, and reprogrammed lipid metabolism towards lipid droplet accumulation, while paradoxically enhancing resilience to ferroptosis inducers. Overall, our findings highlight those essential cellular traits such as ATP production, metabolic activity, oxygen consumption, and cell survival are highly dependent on *TARDBP* function.

1. Introduction

Amyotrophic Lateral Sclerosis (ALS) is a heterogeneous and multifactorial disease characterized by progressive loss of upper and lower motoneurons (MNs) in the brain, brainstem, and spinal cord [1] without disease-modifying treatments. Despite its heterogeneity, there is a common point in approximately 97 % of cases: the appearance of aggregates of ubiquitinated and phosphorylated Transactive response DNA-binding protein 43 (TDP-43) in remaining MNs [2], independently of whether the *TARDBP* gene (encoding for TDP-43) is mutated [3].

TDP-43 is a DNA/RNA binding protein belonging to the heterogeneous ribonucleoprotein family (hnRNPs). It is ubiquitously expressed in all cell types and is essential for embryonic development [4]. Structurally, it is a 43 kDa protein composed of 414 amino acids organized in an N-terminal domain, including nuclear import/export signals, mitochondrial location, and two RNA-recognition motifs that bind to sequences of more than 6000 pre-mRNAs [1]. It exhibits a C-terminal domain that mediates interactions with other hnRNPs through its aggregation-prone (Gln/Asn-rich) sequence, with prion-like properties [5]. Physiologically, TDP-43 is located mainly in the nucleus, although it is also present in the cytoplasm, especially when aggregated [6]. In ALS, TDP-43 is mislocalized from the nucleus and aggregated in the cytoplasm. Whether these aggregates potentially contribute to ALS pathophysiology, by a toxic gain or by a loss of TDP-43 function, is currently unknown. The TDP-43 loss of function might comprise impairment in RNA processing (evidenced as buildup of cryptic exons in selected mRNA [7,8]), energy homeostasis, mitochondrial dysfunction, and oxidative stress [9,10].

Disturbances in energy metabolism -particularly of mitochondrial origin- are also considered pathophysiological hallmarks of ALS. Several studies report the presence of TDP-43 in mitochondria and relate the TDP-43 proteinopathy to mitochondrial defects [11,12]. These misarrangements include changes in mitochondrial dynamics (fission and fusion mechanisms), morphology, distribution and transport, oxidative phosphorylation, and quality control [11]. On the other hand, mitochondria produce high amounts of reactive oxygen species (ROS) as a by-product of cellular respiration [11]. ROS-derived damage is present in spinal cord samples of ALS patients; therefore, ROS is proposed as a

* Corresponding author.
E-mail address: manuel.portero@udl.cat (M. Portero-Otín).

https://doi.org/10.1016/j.redox.2024.103301
Received 4 June 2024; Received in revised form 2 August 2024; Accepted 3 August 2024
Available online 5 August 2024

stress factor implicated in ALS pathophysiology [11]. Whether TDP-43 loss enhances ROS production and impairs cell metabolism is currently unknown.

To solve these caveats, in the present work, we hypothesize that *TARDBP* loss, modeled in both MN and high throughput cellular systems, leads to changes in energy homeostasis, which could be relevant for understanding ALS pathogenesis. Our results show that *TARDBP* silencing, in human induced pluripotent stem cells (hIPSCs) differentiated to MNs, and in an independent system with down-regulable *TARDBP* expression, impair cell survival. We then focused on mitochondrial-related variables showing TDP-43-dependent differences in basal cell metabolism and VO2. In addition, we demonstrate that *TARDBP* silencing in mammalian cells does not impinge a single cell death mechanism explaining the loss of viability together with reprogrammed lipid metabolism towards lipid droplet accumulation. Overall, these results highlight the relevance of TDP-43 in the maintenance of cellular homeostasis and support the use of the proposed cellular model as a potential platform for screening ALS-relevant pathogenic pathways and tentative therapeutic targets.

2. Material and methods

2.1. Cell types and constructs

Human induced pluripotent stem cells (hIPSCs) were used to generate cell-derived MNs. hIPSC control cell line was obtained from NINDS Human Genetics DNA and Cell line Repository at Coriell Institute (ND41865).

HeLa wildtype (Wt) form (obtained from ATCC (#ref CCL-2; HeLa | ATCC)) was used as a control in our experiments. We developed a HeLa cell line expressing an inducible system to knockdown *TARDBP* upon doxycycline exposure employing the Tet-pLKO-puro plasmid (Addgene, Plasmid #21915) [13] expressing a short hairpin RNA (shRNA) targeting *TARDBP* mRNA (Millipore-Sigma TRCN0000016038). Lentiviral particles were produced in HEK293T cell lines transfected with psPAX2 (Addgene, 12260) and pMD2.G (Addgene, 12259) plasmids (both a gift from Dr. Trono) and Tet-pLKO-puro-*TARDBP* for 3 days. Cell medium containing lentiviral particles was collected, centrifuged at 500 relative centrifugal force (RCF) for 5 min, and filtered through a 0.45 μm pore size membrane. HeLa cells were transduced and selected with puromycin at 1 μg/ml. A single clone was isolated to obtain the HeLa pLKO cell line.

For silencing hIPSC-MNs we employed lentiviral transduction. Lentiviral production was produced in HEK293T cells seeded in 100 mm well-plate 24h prior transfection. Transfection protocol was performed following manufacturer's instructions. Briefly, 13 μg of psPAX2 (Addgene, 12260), 7 μg pMD2.G (Addgene, 12259) both a gift from Dr. Trono) and 20 μg of pLVTHM plasmid [14,15] containing shRNA against *TARDBP* or scrambled were mixed by vortex with 120 μL of Fugene HD (E2311, Promega) in 1 mL OptiMEM (31985062, Thermo Scientific) at room temperature for 15 min. Then, the transfection mix was added to HEK293T cells. After 24h of incubation, cell medium was changed with fresh complete medium and incubated for 72h. Finally, cell medium containing lentiviral particles was collected, centrifuged at 500 RCF for 5 min, and filtered through a 0.45 μm pore size membrane.

2.2. Cell culture and treatments

2.2.1. hIPSC-derived motoneurons

hIPSCs were grown in standard human embryonic stem (ES) cell media supplemented with 6 ng/mL basic fibroblast growth factor on inactivated mouse embryonic fibroblasts (MEFs) as feeder cells. Differentiation towards MNs was carried out with a modification of the Du et al. protocol [16] as described in Ref. [17]. Briefly, undifferentiated hIPSCs were digested with Accutase solution (Sigma, A6964) for 5 min, and then the cell suspension was transferred to Geltrex™ (Thermo Scientific, A1413202)-coated cell culture plates. When stem cell colonies were visible media was changed to neuroepithelial media (1:1 DMEM/F12:NeurobasalTM Plus supplemented with 0.2 mM B27+, 1 mM L-glutamine, 1 mM NEAA (Thermo Scientific, 11320033; A3582901; A3582801; 25030081; 11140050), 0.1 mM ascorbic acid (Sigma, A4403), 3 μM CHIR99021, 2 μM SB431512, and 2 μM DMH1 (Cayman Chemical, 13122; 13031; 16679) to generate neuroepithelial cells and then replaced sequentially with MN progenitor 1st and MN progenitor 2nd media (1:1 DMEM/F12:NeurobasalTM Plus supplemented with 0.2 mM B27+, 1 mM l-glutamine, 1 mM NEAA, 0.1 mM ascorbic acid, 1–3 μM CHIR99021, 2 μM SB431512, 2 μM DMH1, 0.1 μM retinoic acid (Sigma, R2625), 0.5 μM purmorphamine (Cayman Chemical, 10009634), and valproic acid (Sigma, P4543)) to generate MN progenitor's 1st and 2nd, respectively.

In each stage of differentiation, which was maintained for a minimum of 6 days, media was changed every other day. Cells were seeded in Geltrex™-coated cell culture plates and split into new Geltrex®-coated dishes when 70%–100 % confluency was achieved, using 10 μM Y27632 (Cayman Chemical, 10005583) during the first 24 h. Then, non-tissue culture dishes without coating were used for neurosphere formation together with MN induction media (1:1 DMEM/F12:NeurobasalTM Plus supplemented with 0.2 mM B27+, 1 mM L-glutamine, 0.1 mM ascorbic acid, 3 μM CHIR99021, 2 μM SB431512, 2 μM DMH1, 0.5 μM retinoic acid, and 0.1 μM purmorphamine)). After 6 days, neurospheres were collected and digested for 5 min in Accumax solution (Sigma, 00-4666-56), until a homogeneous cell suspension was obtained. Cells were then washed with DMEM/F12 (Thermo Fisher, 11320033) and re-suspended for seeding in MN maturation media (1:1 DMEM/F12:NeurobasalTM Plus supplemented with 0.2 mM B27+, 1 mM L-glutamine, 0.1 mM ascorbic acid, 0.5 μM retinoic acid, 0.1 μM purmorphamine, 20 ng/mL CNTF (Peprotech, 450-13), and 20 ng/mL IGF1 (Thermo Scientific, 11682069)) supplemented with 10 μM Y27632, and 0.1 μM Compound-E (Stem Cell Technologies, 73952) to generate MNs. Finally, MNs were seeded in poly-L-ornithine (Sigma, P4957) and laminin (Sigma, L2020) coated dishes.

Cells were counted using the LUNA-II Automated Cell Counter (Logos Biosystems). For experiments, MNs were seeded at 80000 cells/well in 4-well plates for Western blot analysis, 500000 cells/well in 6-well-plate for qRT-PCR experiments, 20000 cells/well in 96 multi-well plates and in Seahorse cell culture plates.

For lentiviral transduction, the medium containing lentivirus was added 2 h after neurosphere seeding. The medium was changed 24 h later and infection efficiency was monitored in each experiment by direct counting of GFP-positive cells.

2.2.2. HeLa cell line

Both Wt and pLKO HeLa cells were maintained in complete medium containing Dulbecco's Modified Eagle's medium (DMEM) (Gibco, Invitrogen 41965-039) with 4.5 g/L glucose, 2 mM glutamine, 1 % sodium pyruvate (Gibco, Invitrogen 11360-039), 10 % Fetal Bovine Serum (FBS) (Gibco, Invitrogen 10438018), 1X Antibiotic Antimycotic (Gibco, Invitrogen 15240-062) and 0.1X Plasmocin prophylactic treatment (InvivoGen, ant-mpp). Cells were split every 2–3 days (at 70–90 % confluency) and incubated at 37 °C in a humidified environment with 5 % CO2. We employed doxycycline (200 ng/mL) to the cell culture media for 72 h to induce *TARDBP* silencing. In selected experiments we employed shorter times.

HeLa cells were seeded in multi-well plates for stress-inducing experiments and counted using the LUNA-II Automated Cell Counter (Logos Biosystems). For seeding the 96 multi-well plates and performing the stress experiments we used the semi-automatic device Opentrons Robot (OT-2 model) connected to a HEPA filter system. Ferroptosis stress experiments were performed by exposing cells to known inducers of ferroptosis (Erastin (MERCK, 329600) and RSL-3 (SIGMA, SML2234); to known inhibitor (Ferrostatin (MERCK, SML0583)); or dimethyl sulfoxide (DMSO) (Thermo Scientific, D12345) as vehicle), in complete

DMEM. We used staurosporine (FOCUS, 10–214) as positive control of cell death and untreated cells as negative control.

2.3. Prestoblue cell viability assay

PrestoBlue™ Cell Viability Reagent (Invitrogen, A13262) was used to assess cell viability. This assay quantifies cell viability based on the reducing power of living cells, which is secondary to its metabolic activity. PrestoBlue™ reagent was added at a ratio of 1:10, and cells were incubated for 1h at 37 °C in a humidified environment with 5 % CO2. After incubation, samples were read using a fluorescence microplate reader (Infinite M200, TECAN) at 560/590 nm excitation/emission wavelengths.

2.4. Crystal violet cell viability assay

As resazurin based assays such as Prestoblue™ above are affected by viability independent effects in metabolic constraints, we also employed the crystal violet assay [18]. Briefly, after the corresponding experimental conditions, the medium was removed, and cells were washed twice with PBS. Then, cells were incubated for 20 min with Crystal Violet 0.2 % in ethanol (Sigma, C0775). After incubation, cells were washed 5 times with PBS and allowed to dry. Finally, 100 μL of 1 % sodium dodecyl sulfate (SDS) was added. Absorbance of each well was measured using a microplate spectrophotometer (Epoch, BioTek) at 570 nm.

2.5. Flow cytometry analysis

We used flow cytometry as a measure of cell viability, differentiating cells between proliferating and dead, and between apoptotic and other types of cell death by two different fluorescent labels: the Fluorogenic substrate CellEvent™ Caspase-3/7 Green Detection Reagent (Thermo Scientific, Invitrogen, C10423); and Propidium Iodide (PI) (Thermo Scientific, Invitrogen, P1304MP). We also measured superoxide production by MitoSOX™ (Thermo Scientific, Invitrogen, M36008) and mitochondrial membrane potential by Image-iT™ TMRM (Thermo Scientific, Invitrogen, I34361). Samples were analyzed by FACS Canto II Flow Cytometer (Becton Dickinson).

For viability analysis, we collected both live (adherent) and dead (floating) cells, centrifuged them at 1500 RPM (revolutions *per* minute) for 15 min, and resuspended the pellet with 100 μL of PBS supplemented with 2 % FBS together with two drops/mL of Fluorogenic substrate CellEvent™ Caspase-3/7 Green Detection Reagent. After 30 min incubation at 37 °C, we added 100 μL of PBS supplemented with 2 % FBS and incubated them 5 min at room temperature with 1.25 μg/mL of Propidium Iodide.

For superoxide and mitochondrial membrane potential analysis, we collected adherent cells, centrifuged them 1500 RPM for 15 min, and resuspended the pellet with 100 μL of PBS supplemented with 2 % FBS and incubated them 30 min at 37 °C with 1 μM of MitoSOX™ reagent or 200 nM of Image-iT™ TMRM, respectively.

2.6. Continuous oxygen consumption measurement

Cellular oxygen consumption rates (OCR) were measured employing a Resipher multi-well dynamic oxygen consumption reader. The system employs proprietary, ultra-sensitive oxygen sensors, evaluating every 30 min the dissolved oxygen concentration gradient formed by metabolically active cells at the bottom of the well. The declared consumption resolution is 5 fmol/mm2/sec, with concentration sensitivity <1 μM. Briefly, cells were seeded on 96 multi-well plates for 30 min before experimentation. Then, the Resipher oxygen sensing lid (Lucid Scientific) was attached. We analyzed data on the Resipher web application (https://lab.lucidsci.com).

2.7. High-content cell respiration phenotype measurement

Cell respiration phenotype was determined by Agilent Seahorse XF Cell Mito Stress Kit (103015-100; Agilent Technologies) following manufacturer's instructions. Short-term (<3h) OCR and medium pH were determined in a Seahorse XFp analyzer. 1h before treatment completion, the cellular medium was changed to Seahorse XF DMEM medium supplemented with 25 mM glucose, 1 mM pyruvate, and 2 mM glutamine. The assay protocol consisted of 3 measurements at each stage, starting with basal respiration, followed by the injection of Oligomycin (1.5 μM), Carbonyl cyanide-*p*-trifluoromethoxyphenylhydrazone (FCCP) (1.0 μM), and Rotenone/Antimycin A (0.5 μM of each compound). After the analysis, cell content in each well was normalized by Crystal Violet staining assay.

2.8. Rescue experiments (TARDBP transfection protocol)

For the transfection of wt*TARDBP* and Δm1*TARDBP* DNA-containing plasmids we used Lipofectamine 3000 (Thermo Scientific, L3000008) (sequences of both plasmids are shown in Supplementary Table 1). The protocol was performed following the manufacturer's instructions. Lipofectamine and p3000 reagent were both diluted into Opti-MEM™ (Thermo Scientific, 31985070). p3000 reagent was mixed with the DNA plasmids and lipofectamine and incubated at room temperature for 25 min. The resulting mix was added to the cells, and after 24h, the medium was changed. Finally, cells were harvested for downstream analysis 48h after transfection. The amount of DNA plasmids and consequently the amount of lipofectamine and p3000 reagent were different depending on the well-plate used. GFP DNA plasmid was used as a transfection control in all the experiments.

2.9. Fluorescence stainings

Cell nuclei were stained with NacBlue™ Live Cell Stain ReadyProbes™ reagent (Invitrogen, R37605). Mitochondria were stained using MitoTracker™ Green FM (Invitrogen, M7514). Superoxide production in mitochondria was estimated with MitoSOX™ Red Mitochondrial Superoxide Indicator (Invitrogen, M36008). Mitochondrial membrane potential was stained with Image-iT™ TMRM (Thermo Scientific, Invitrogen, I34361). Neutral lipids were stained using LipidTOX™ (Fisher Scientific, H34475). Lipid droplets (LD) were stained using Nile Red (MERCK, N3013). Mitotracker™ ~~and~~ MitoSOX™ and Image-iT™ TMRM staining were performed in living cells. LipidTOX™ and Nile Red staining were performed in fixed cells with paraformaldehyde (PFA). All staining reagents were diluted in Hank's Balanced Salt Solution (HBSS) (Thermo Scientific, 14025092). For fixation cells were incubated with 4 % PFA for 15 min at room temperature. Incubation time, doses, and temperature (shown in Supplementary Table 2) varied depending on the staining. After incubation, stainings were washed with HBSS 3 times. Imaging was performed with fluorescence microscopy. Images were quantified employing Cell Profiler [19]. Pipelines and images are available online (10.6084/m9.figshare.22137515).

2.10. Immunoblotting

Cell lysates were obtained by recovering dead floating and adherent cells, and mixed with RIPA lysis buffer (MERCK, R0278) supplemented with 1X Protease Inhibitor Cocktail (Thermo Scientific, 78429), 1 mM protease and phosphatase inhibitors (sodium fluoride (NaF) (MERCK, 201154) and sodium orthovanadate (Na3VO4) (MERCK, S6508)). After sonication, protein quantification was performed by the Bradford assay (Bio-Rad Protein Assay Kit I, 5000001)). Following sodium dodecyl sulfate and beta-mercaptoethanol addition and thermic treatment (95 °C, 5 min), samples containing 15 μg of protein were resolved on SurePAGE™ Precast gels (4–20 %, 15 wells GenScript) by Sodium Dodecyl Sulfate Polyacrylamide Gel Electrophoresis (SDS-PAGE) and

transferred to Polyvinylidene Difluoride (PVDF) membranes with EZ-Transfer device (GenScript). Membranes were blocked with I-Block (Thermo Scientific, T2015) for 1h and incubated with primary antibody overnight at 4 °C and secondary antibody for 1h at room temperature. Immunoreactivity was developed by chemiluminescent detection with Immobilon™ ECL Ultra Western HRP Substrate (Merck Millipore, WBKLS0500) and visualized using a Chemidoc MP Imaging System (Bio-Rad). Finally, membranes were stained with Coomassie Brilliant Blue G (Sigma-Aldrich, 27815) for normalization, and specific bands were quantified by ImageLab software (Bio-Rad, version 6.1). Raw blots are available in the supplementary material online.

Primary antibodies targeted TDP-43 (Protein Calbiochem, 474790, 1:1000), PFKP (Atlas Antibodies, HPA018257), ACSL4 (MERCK, HPA005552, 1:10000), GPX4 (SantaCruz, sc-166570), TfR1 (Thermo Scientific, 13–6800), PARP-1 (Thermo Scientific, PA5-27219, 1:1000), cleaved-Caspase 3 (Cell Signalling Technology, 92570, 1:1000), RIPK-1 (Cell Signalling Technology, 92570, 1:1000), phosphorylated MLKL (Cell Signalling Technology, 92570, 1:1000), OxPhos (Thermo Scientific, 45–8199, 1:20000), OPA1 (Millipore, ABN95, 1:1000), FIS1 (Thermo Scientific, PA1-41082, 1:1000). Secondary antibodies used were anti-Rabbit IgG (Invitrogen, 31460, 1:40000) and anti-Mouse IgG (MERCK, NA931, 1:40000).

2.11. Quantitative Reverse Transcription PCR (RT-qPCR)

RNA was extracted from cells using TRI Reagent (Thermo Scientific, AM9738) following the manufacturer's instructions. RNA concentration was measured using a NanoDrop ND-1000 (Thermo Scientific). 2 μg RNA were used for retrotranscription to cDNA employing the StaRT Reverse Transcription kit (AnyGenes, StaRT-25). qPCR experiments were performed using the CFX96 instrument (Bio-Rad) and qPCR Perfect Master Mix SYBR® Green (AnyGenes, PMSX-W12S). RT-qPCR run protocol was as follows: 95 °C for 10 min for initial denaturation; 95 °C for 10 s and 60 °C for 30 s (during 45 cycles) for amplification, and 95 °C for 10 s and 65 °C for 30 s for melting curve. Primers employed were purchased at AnyGenes, otherwise are listed in Supplementary Table 3.

2.12. ELISA

We used the Human Neurofilament Light Chain ELISA Kit (MyBioSource) for the quantitative detection of Human Neurofilament Light Chain (NFL) in the supernatant of hIPSC-MNs following the manufacturer's instructions. Briefly, we added 10 μl anti-NFL antibody to the sample, then 50 μl streptavidin-HRP and incubated for 60 min at 37 °C. After, we washed the plate 5 times with a wash buffer. Then, we added 50 μl substrate solution A and 50 μl substrate solution B and incubated for 10 min at 37 °C in the dark. Finally, we added 50 μl Stop Solution and determined the optical density (OD value) using a microplate reader at 450 nm.

2.13. Triglyceride, Glycerol and Total Lipids assays

For Triglyceride, Glycerol and Total Lipids determination we used total homogenate sample from HeLa pLKO cells. Adherent cells were harvested using a cell scraper, diluted in PBS and sonicated for homogenization.

2.13.1. Triglyceride (TAG) content was determined by a colorimetric assay (SPINREACT, 1001310) based on chain reaction from triglycerides incubated with lipoproteinlipase which liberates glycerol and free fatty acids. In the final step hydrogen peroxide reacts with 4-aminophenazone and *p*-chlorophenol in presence of peroxidase producing red color.

2.13.2. Glycerol content was determined by a Glycerol Assay Kit (Sigma, MAK117) which is based on a coupled enzyme fluorometric assay (glycerol kinase and glycerol phosphate oxidase).

2.13.3. Total lipid content was determined by a colorimetric assay (SPINREACT, 1001270) based on phosphovainilline color change to pink of carbonium ions produced by unsaturated lipid reaction with sulphuric acid.

2.14. Transmission electron microscopy (TEM)

Transmission electron microscopy (TEM) was performed as previously described [20] to asses' mitochondrial morphological traits. Briefly, cells were collected, fixed (0.1 M phosphate, 2.5 % glutaraldehyde, 2.5 % PFA) and incubated 2 h at 4 °C. After fixation, cells were postfixed in 1 % OsO4 for 2 h and then contrasted with 0.5 % uranyl acetate for 30 min. Samples were processed for Embed 812 (Electron Microscopy Sciences, Hatfield, PA, USA) epoxy resin according to standard procedures. Semithin transversal sections (1 μm thick) were stained with Richardson stain and imaged using an Olympus × 60/1.4NA PlanApo oil immersion objective (Olympus) and a DMX 1200 Nikon (Tokyo, Japan) digital camera. Ultrathin sections were counterstained with Reynold's lead citrate. All observations were performed on a transmission electron microscope JEOL JEM 1400 (Akishima, Tokyo, Japan). Mitochondrial morphologies were quantified as indicated [21] in a double blinded fashion, quantifying at least 30 different cells in each condition. Briefly, the morphology of mitochondria was measured using open-source software Image J, obtaining mitochondrial length, width, area and circularity.

2.15. Statistical analysis

All statistical analyses and figures were performed by GraphPad Prism software (GraphPad, v.9.4.0). Differences between groups were analyzed by Student's t-test, one-way or two-way analysis of variance (ANOVA), followed by corresponding post hoc analysis where applicable. Unless stated otherwise, data are expressed as means ± SEM with minimal statistical significance established as 0.05.

3. Results

3.1. TARDBP silencing results in a lack of metabolic activity linked to diminished VO2 and cell viability

We modeled TDP-43 loss-of-function, employing hIPSC-MNs, where *TARDBP* was silenced by lentiviral infection, achieving approximately 50 % of TDP-43 expression after 6 days of transduction (Fig. 1A). In line with previous results [15], depletion of TDP-43 in hIPSC-MNs resulted in the buildup of cryptic exons in ATG4b and GPSM2 (Fig. S1) and, interestingly, PFKP mRNAs, without significant effects in PFKP protein (Fig. 1A). Moreover, loss of TDP-43 induced neurite degeneration (Fig. 1B) and significant reductions both in metabolic activity (i.e., PrestoBlue™ reagent), and in cell viability (i.e., crystal violet assay), resulting in the release of neurofilaments (Fig. 1C). In addition, continuous VO2 monitoring (Fig. 1D) showed that *TARDBP* silencing led to a significant decrease after 5 days of transduction.

To evaluate if these results were cell-type independent, avoiding off-target effects of viral transduction, and to offer a faster turnaround model, we generated a HeLa clone (from now on pLKO) showing inducible loss of *TARDBP* expression when exposed to doxycycline, resulting in almost no TDP-43 after 72h (Fig. 1E). Accordingly, to hIPSCs-MNs, *TARDBP* loss in pLKO cells resulted in the buildup of cryptic exons in ATG4b, GPSM2 and, PFKP mRNAs, together with a decrease in the levels of total PFKP mRNA (Fig. S1).

Validating its use as MN surrogates, TDP-43 loss was associated with changes in cell morphology (Fig. 1F), metabolic activity, and cell viability (Fig. 1G) that paralleled the loss of *TARDBP* expression in hIPSC-MNs. Reproducing MN results, the pLKO showed a significant VO2 decrease (Fig. 1H). The VO2 early decrease at the first 24–48 h (when the levels of TDP-43 are still high), is also observed in metabolic

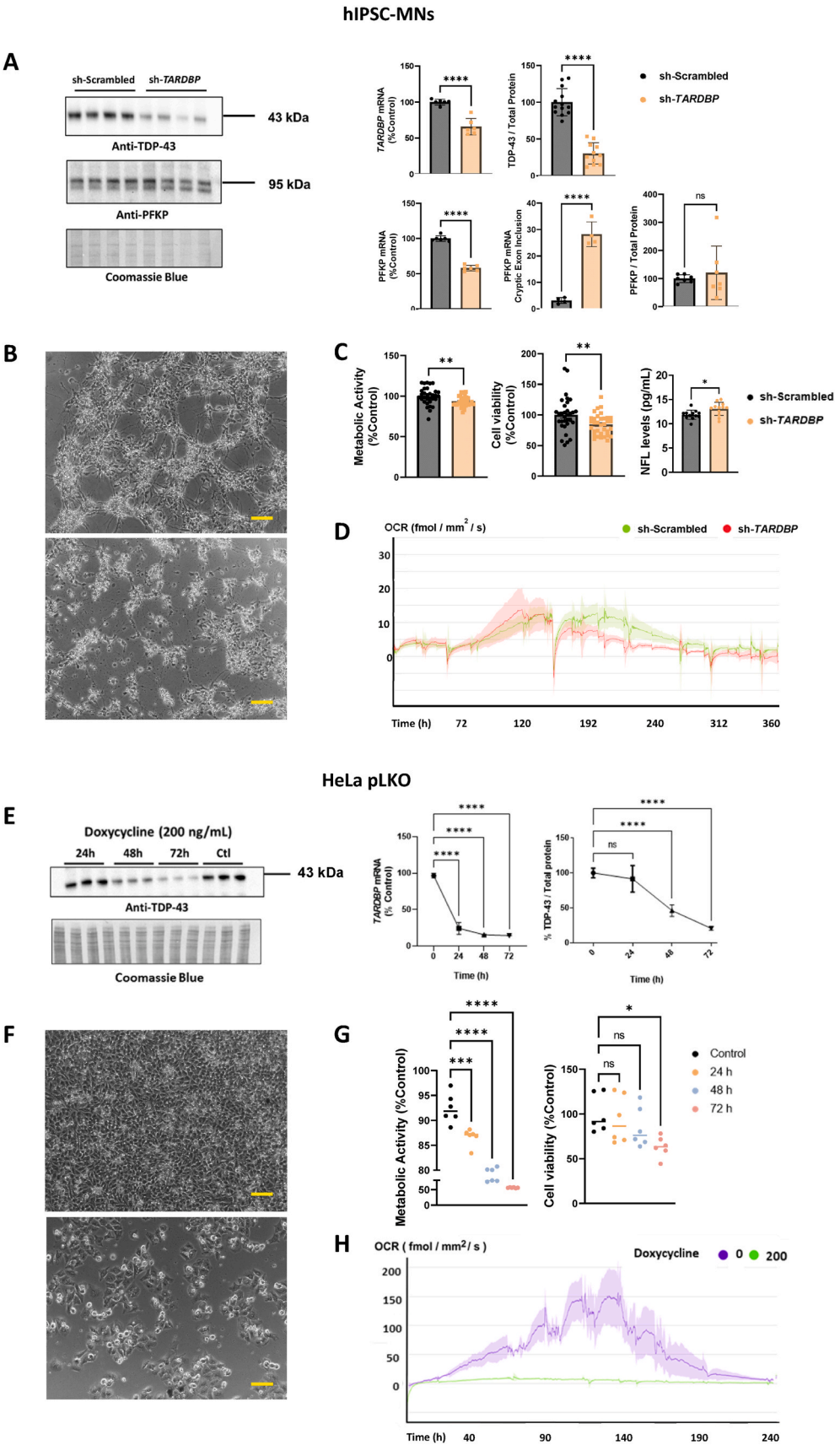

(caption on next page)

Fig. 1. TDP-43 loss impairs cellular metabolic activity and VO2.
(A) TARDBP and PFKP mRNA, and protein levels of hIPSC-MNs 6 days after transduction with sh-scrambled or sh-TARDBP. For PFKP, the percentage of cryptic exon inclusion is also shown. (B) Morphological changes of hIPSC-MNs 6 days after transduction with sh-scrambled (upper) and sh-TARDBP (lower). (C) Metabolic activity (left); Cell viability (middle); and Neurofilament levels (pg/mL) on supernatants (right) of hIPSC-MNs 6 days after transduction with sh-scrambled or sh-TARDBP. (D) OCR of hIPSC-MNs 15 days after transduction with sh-scrambled or sh-TARDBP. (E) TARDBP mRNA and protein levels of pLKO cells after a time course treatment (doxycycline 200 ng/mL). (F) Morphological changes of pLKO cells untreated (upper) and doxycycline (200 ng/mL) treated (lower). (G) Time course of metabolic activity (left) and cell viability (right) of pLKO cells (doxycycline 200 ng/mL). (H) OCR of pLKO cells un/treated with doxycycline (200 ng/mL) for 240 h. 0: untreated; 200: 200 ng/mL doxycycline. In (A) and (B) differences between sh-Scrambled and sh-TARDBP were analyzed by Student's t-test. In (C) and (G) cells scale bar: 20 μm. In OCR measurements (D) and (H) shadows of profiles indicate a 95 % confidence interval for measured data. In (E) and (F) differences between time points are analyzed by paired one-way ANOVA and Dunnett's-corrected multiple comparisons test. All western-blot analyses were normalized to protein content, measured by densitometric analysis of total protein load by Coomassie Blue staining. *, **, *** and **** indicate, respectively $p < 0.05$, $p < 0.01$, $p < 0.001$, and $p < 0.0001$. (For interpretation of the references to color in this figure legend, the reader is referred to the Web version of this article.)

activity but not for cell viability (Fig. 1G) probably reflecting off-target effects of doxycycline on cell's reducing capacity [22].

To further characterize metabolic phenotype of *TARDBP* silencing, we employed high content respirometry (i.e., the Mito Stress test in Seahorse™ apparatus). In hIPSC-MNs, in line with continuous OCR measurements, *TARDBP* silencing affected both basal VO2 and mitochondrial responses to oligomycin and FCCP (Fig. 2A), resulting in a switch in the bioenergetic profile towards glycolysis (Fig. 2B). When analyzing integrated results, *TARDBP*-silenced hIPSC-MNs had increased VO2, not coupled to ATP production (Fig. 2C). Similarly, we performed high content respirometry in pLKO cells. While the effects of *TARDBP* silencing in basal VO2 were different from in hIPSC-MNs (Fig. 2D), it induced a shift towards glycolysis and loss of mitochondrial spare capacity (i.e., difference of basal respiration respect to maximal OCR) which was common with hIPSC-MNs (Fig. 2E). As shown in hIPSC-MNs, *TARDBP* silencing was associated with decreased ATP production (Fig. 2F), suggesting that *TARDBP* silencing induces a loss in mitochondrial fitness (i.e., ATP production related VO2) and flexibility (i.e., capability of the cell to respond to an energetic demand).

Anti-porin Western blot and Mitotracker™ staining excluded a loss in mitochondrial mass or gross changes in fission/fusion (Fig. S1) as a main mechanism for these changes. We then evaluated, by TEM, the ultrastructure of mitochondria. The results (Fig. 3A) indicate that mitochondrial mass is not affected by doxycycline treatment. Rather, larger and rounder mitochondria are found in *TARDBP* silenced cells (Fig. 3B). Indeed, several images compatible with defective mitophagy/altered endoplasmic reticulum with enhanced fragmentation were evident in this later situation (Fig. 3A, inset). To further quantify the mitochondrial impairment, we quantified the mitochondrial potential by TMRM through flow cytometry (Fig. 3C). *TARDBP* silencing resulted in the buildup of a cell population with a major loss of mitochondrial membrane potential, without major changes in mitochondrial mass (Fig. 3C). Defective mitochondria can show enhanced free radical production. We estimated free radical production by MitoSOX™. The results (Fig. 3D and E) indicate that *TARDBP* loss enhanced free radical production. Indeed, other measures of mitochondrial function, such as the content of representative peptides of respiratory complexes (Fig. 3F) did not disclose a major effect derived from *TARDBP* loss.

3.2. Transfection of wtTARDBP and Δm1TARDBP in pLKO cells restores TDP-43 expression but fails to recover metabolic deficits

Given the mitochondrial functional phenotype derived from the loss of function of TDP-43, we transfected pLKO cells, after doxycycline treatment, with wt*TARDBP* to potentially rescue them. We employed a form of *TARDBP* (from now on Δm1*TARDBP*) lacking an internal motif spanning from the 35 to the 41 residues (FPGACGL) required for mitochondrial import [23], to evaluate the need of TDP-43 translocation to mitochondria. The results show that, after wt*TARDBP* or Δm1*TARDBP* transfection, we recovered doxycycline induced loss of expression of TDP-43 (Fig. 4A). Interestingly, Δm1*TARDBP* transfection induced the accrual of low molecular weight (ca 25 KDa) C-terminal fragments of TDP-43. Despite *TARDBP* overexpression did not associate to changes in overall metabolic reducing activity nor cell viability (Fig. 4B), it was able to recover continuous OCR and cell duplication, requiring mitochondrial location for this recovery (Fig. 4C), as Δm1*TARDBP* did not produce equivalent results. Indeed, wt*TARDBP* (and to a minor extent Δm1*TARDBP*) transfection rescued loss in basal VO2 as well as in ATP-linked O_2 consumption (Fig. 4D and F). These rescue experiments show that bioenergetic metabolism was recovered by *TARDBP*, dependent on its mitochondrial location (Fig. 4E), resulting in a less quiescent phenotype. Thus, TDP-43 transfection increased VO2 and acidification capacities, with mitochondrial location being required, probably linked to increased proliferative capacity.

3.3. TARDBP loss induces an apoptosis-independent cell death in pLKO cells and a potential build-up of lipid droplets

To evaluate if *TARDBP* silencing enhanced cell death, we measured propidium iodide (PI) and caspase 3/7 staining -markers of global cell death and apoptosis, respectively-by flow cytometry. As shown in Fig. 5A, pLKO cells showed mortality values around 10 % of the total cell population in control conditions, meanwhile doxycycline treatment induced a significant increase in cell mortality (up to 30 %). Apoptosis, measured as caspase 3/7 positivity, was a residual phenomenon in these conditions (below 2 % of the cell population (Fig. S2). Despite the cells showing capacity for this modality of cell death, based on staurosporine response, none of the apoptosis inhibitors evaluated - Q-VD and Z-VD - recovered the viability after *TARDBP* silencing (Fig. S2). In agreement with the low levels of apoptosis obtained by flow cytometry, we did not observe increased expression levels of cleaved caspase 3 and Poly ADP-ribose polymerase 1 (PARP-1) (89 kDa) (Fig. S2), indicating that silencing of *TARDBP* leads to caspase-3/7 independent cell death.

Once apoptosis was ruled out as the main cause of cell death, we analyzed other pathways of programmed cell death. We observed that the expression of receptor-interacting serine/threonine-protein kinase 1 (RIPK-1) and mixed lineage kinase domain-like pseudokinase (MLKL) proteins - involved in the necroptosis pathway [24]- was not different in control and *TARDBP*-silenced cells (Fig. S2) confirming the well-known necroptosis resistance of HeLa [25]. On the other hand, we found increased levels of long-chain-fatty-acid—CoA ligase 4 (ACSL4), and decreased glutathione peroxidase 4 (GPX4) compatible with ferroptosis, though transferrin receptor protein 1 (TfR1) was unchanged (Fig. 5B). At the mRNA level, *TARDBP* silencing was not clearly associated with an expression pattern of classical ferroptosis [26]. Thus, *TARDBP* silencing increased ACSL4 expression and decreased SLC7A11 mRNA, but decreased other hallmarks of ferroptosis, such as CHAC1 mRNA levels (Fig. 5C). Also, *TARDBP* silencing decreased the expression of genes related to iron metabolism (Fig. 5C). To confirm the sensitivity of this model to ferroptosis, we performed experiments on well-known inducers of this death pathway, such as Erastin (Xc-system inhibitor) and RSL-3 (GPX4 inhibitor), and an inhibitor, Ferrostatin. As shown in Fig. 5D, Erastin and RSL-3 decreased significantly metabolic activity in pLKO cells compared to the vehicle DMSO, with the combination of both reagents producing a higher decrease. When evaluating the influence of *TARDBP*, we found that its loss did not increase sensitivity to these

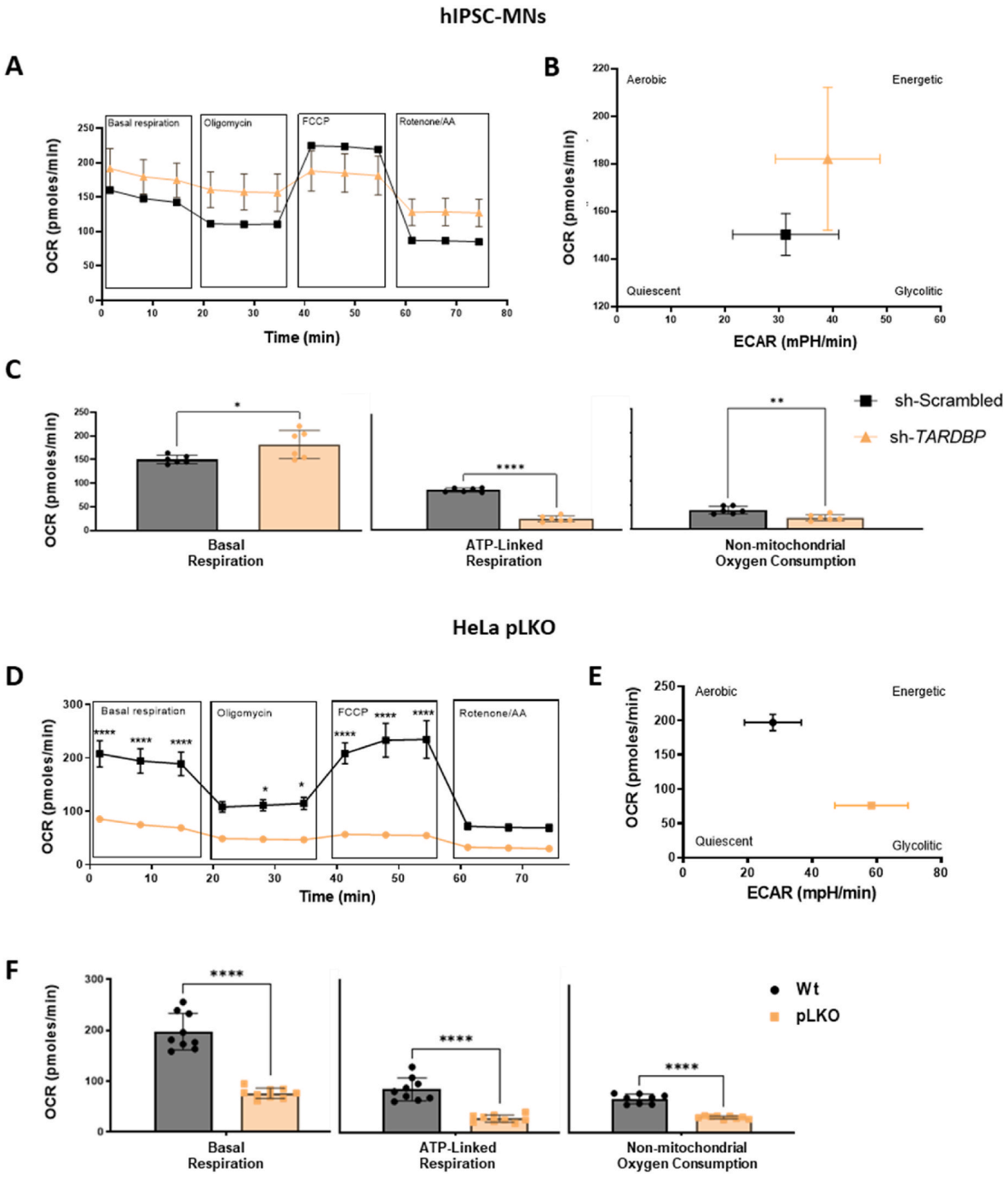

Fig. 2. TARDBP loss causes a shift in mitochondrial metabolism in association with lower proliferative rates.
(A) OCR employing the Seahorse™ apparatus, normalized for cell number, of hIPSC-MNs after 6 days transduction with sh-scrambled or sh-TARDBP. Cellular respiration phenotype protocol included three measurements at each stage: 1- Basal respiration; 2-Oligomycin (1.5 μM); 3-FCCP (1.0 μM); 3-Rotenone/Antimycin A (0.5 μM each compound). (B) Energy Map of hIPSC-MNs after 6 days transduction with sh-scrambled or sh-TARDBP. (C) sh-scrambled and sh-TARDBP hIPSC-MNs differences in OCR during basal respiration, ATP-linked respiration, and non-mitochondrial oxygen consumption (D) OCR employing the Seahorse™ apparatus, normalized for cell number, of Wt and pLKO cells treated with doxycycline (200 ng/mL) for 72h. (E) Energy Map of Wt and pLKO cells treated with doxycycline (200 ng/mL) for 72h. (F) Wt and pLKO treated with doxycycline (200 ng/mL) 72h differences in OCR during basal respiration, ATP-linked respiration, and non-mitochondrial oxygen consumption, respectively pLKO values are referred to as incremental or decremental behavior compared with Wt. Differences in the OCR were determined by two-way ANOVA and Sidak's-corrected for multiple comparison tests, with other differences being analyzed by Student's t-test ($p < 0.0001$). *, **, *** and **** indicate, respectively $p < 0.05$, $p < 0.01$, $p < 0.001$, and $p < 0.0001$.

inducers (Fig. 5D). Moreover, inhibitor Ferrostatin did not recover cell viability in any condition (Fig. 5D).

Since increased ACSL4, whose main action is conjugating CoA for lipid biosynthesis and fatty acid degradation, might not be entirely explained to ferroptosis, we focused on its role as lipid metabolism intermediate. Indeed, we found that *TARDBP* silencing enhanced neutral lipid buildup, such as lipid droplets (LD), measured by two different reagents (Fig. 5E). Despite these imaging analyses, biochemical evidence of increased lipid amount and triacylclyceride contents was not found (Fig. 5F), despite a slight decrease in glycerol content was evident

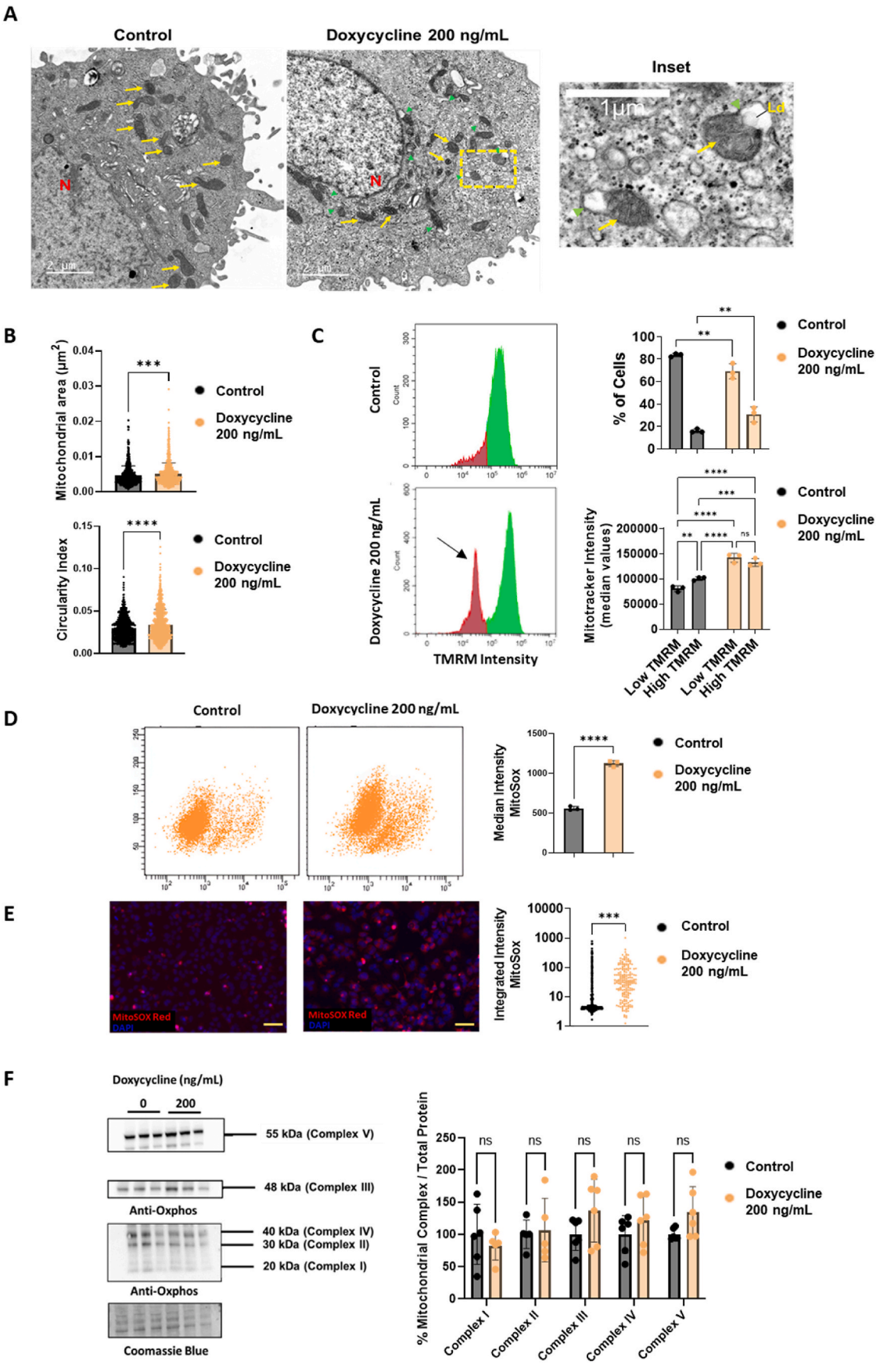

(caption on next page)

Fig. 3. TARDBP silencing impaired mitochondrial function, with increased ROS production and no major ultrastructural changes.
(A) Representative TEM images of mitochondria in pLKO cells un/treated with doxycycline (200 ng/mL) for 72h. Right inset shows amplification of marked square. In TEM micrographs, yellow arrows indicate mitochondria while green arrowheads show images compatible with autophagy vesicles in contact with mitochondria. N: Nuclei, Ld: lipid droplet-compatible structure. (B) Mitochondrial area (per square micrometer) and circularity indexes quantified as indicated in Methods section (n = 30 images per condition quantified). (C) TMRM intensity after flow cytometry analyses. Right panel show percentage of cells and Mitotracker™ fluorescence intensity, showing a cell population with lower mitochondrial potential (marked by an arrow) in pLKO cells after doxycycline (200 ng/mL) exposure for 72h. (D) Representative scatter plot of flow cytometry analysis of pLKO cells un/treated with doxycycline (200 ng/mL) for 72h (left) and MitoSox™ median intensity (right). (E) Fluorescence microscopy of Wt and pLKO living cells treated with doxycycline (200 ng/mL) for 72h. Nuclei (in blue) were stained with NacBlue™. Superoxide (in red) was estimated with MitoSox™. The right panels show the integrated intensity of MitoSox™. Scale bar: 20 μm. (F) Representative western-blot (left panels) and densitometry (right panels) of electron transport chain complexes after 72h doxycycline (200 ng/mL) treatment in pLKO cells. In (B), (D) and (E) differences were analyzed by Student's t-test. In (C) and (F) differences were analyzed by two-way ANOVA and Sidak's-corrected multiple comparisons test. All western-blot analyses were normalized to protein content, measured by densitometric analysis of total protein load by Coomassie Blue staining. *, **, *** and **** indicate $p<0.05$, $p<0.01$, $p<0.001$ and 0.0001. (For interpretation of the references to color in this figure legend, the reader is referred to the Web version of this article.)

(Fig. 5F). Globally these results mainly rule out apoptosis and ferroptosis as the main contributors to *TARDBP*-dependent cell death and suggest that cellular lipid metabolism is impacted by *TARDBP* loss as it potentially enhances LD accumulation, fueled by ACSL4 increased expression.

4. Discussion

Due to the implication of neuronal and glial dysmetabolism in ALS [10], we hypothesized that loss of TDP-43 function could have bioenergetic consequences. The present results confirm that decreased *TARDBP* expression leads to both cell viability-loss and enhanced probability of non-apoptotic cell death. Mitochondrial defects appear to partially mediate these effects, as *TARDBP* rescue experiments were able to correct mitochondrial-dependent OCR and ATP production but failed to fully recover cell viability in our system. Interestingly, at least in the HeLa context, *TARDBP* loss produced a buildup of LD-like particles, in line with increased ACSL4 expression, with a decreased sensitivity to ferroptosis susceptibility despite increased free radical production. Overall, main effects on viability seems quite independent on cell type and system to silence, as it is present both lentiviral transduced hIPSC-MNs and doxycycline-inducible HeLa pLKO. *TARDBP* silenced hIPSC-MNs modeled neurodegeneration as evidenced by increased neurofilament in media (suggestive of neuronal lysis), the buildup of cryptic exons, and neurite degeneration. Since the selected HeLa-derived clone showed similar behavior in basic cell physiology (i.e., OCR and ATP-production) we propose the use of this clone as a potential, high-throughput, tool for the study of *TARDBP* loss in cell physiology.

We integrated several indicators of cell physiology related to energy metabolism, a resazurin-based cell viability reagent, continuous OCR, high-content respirometry, crystal violet and PI staining. Despite globally the effect of *TARDBP* loss on most of these variables converging, a more accurate view showed some divergences across these readouts of cell health. These differences support the need for a multifaceted approach when studying the cellular effects of the loss of a pleiotropic factor as *TARDBP*. As a potential limitation, doxycycline treatment at the assayed doses, in the parental HeLa cell line, led to a partial decrease in metabolic activity and OCR values (data not shown), reflecting off-target effects of doxycycline [22]. Tetracyclines, as doxycycline, are known for modifying human ribosomal translation and selectively activating the cellular integrated stress response. Previous data from our lab and others show that cell stress impinges TDP-43 disarrangements [27], in agreement with recent data showing that translational stress is involved in ALS [28]. Therefore, our data in the pLKO clone are partly compatible with doxycycline -at doses employed-interacting with TDP-43 loss, both impinging ribosomal stress and explaining the loss of viability. All in all, even accounting this off-target effect, the fact that hIPSC-MNs, in a doxycycline-independent experimental setup, also show decrease in metabolic activity (measured as reducing capacity, continuous and high-content OCR) in conditions of *TARDBP* loss, reinforce the robustness of the pLKO results and the potential of this approach as a screening system, in comparison to the more resource- and time-consuming hIPSC-MNs.

Data presented here in OCR and mitochondrial misarrangaments fully agree with data showing that TDP-43 proteinopathy associates with loss of ATP production (P. [12]). We propose that TDP-43 aggregation-induced functional loss (e.g., by sequestering monomeric TDP-43) might contribute to oxidative phosphorylation impairment present in ALS models [29–31]. Of note, ultrastructural and flow cytometry measurement suggest that these changes are not present in all cells, demonstrating a non-negligible heterogeneity (e.g. in case of TMRM analyses). Also, in the pLKO cells, alterations in mitophagy could contribute to explain oxidative stress [15,32]. In pLKO cells, doxycycline-derived sharp decreases in both, metabolic activity and cellular respiration, were not immediately nor fully prevented by liposome-mediated *TARDBP* overexpression. Asides from the above indicated doxycycline off target, this apparent paradox may be explained by the fact that VO2-coupled ATP production in pLKO is strongly dependent on *TARDBP*, while cellular viability might require further time or other characteristics to be fully rescued. We should indicate that Δm1*TARDBP*, in addition to its inefficacy to recover continuous OCR decrease impinged by *TARDBP* loss, enhances the formation of 25 KDa C-terminal fragments, that in other contexts, have been associated to cell toxicity [33–35]. Similarly, we cannot exclude that *TARDBP* overexpression would have other deleterious consequences, in line with its excess also having negative consequences and the need for a fine-tuned regulation [36]. Noteworthy, *TARDBP* promoter is under the control of TDP-43 activity, ensuring a control for potential excess [36]. Overall, our results show that metabolic effects of TDP-43 loss are pleiotropic, leading to inefficiencies of ATP production, OCR, and metabolic activity. These inefficiencies are associated with increased free radical production and consequent cell death, supporting that TDP-43 function is necessary for maintaining adequate energetic homeostasis.

Regarding cell death pathways induced by *TARDBP* silencing, we found a high value of cell lethality (i.e., measured by propidium iodide positivity) in pLKO after doxycycline treatment. The occurrence of canonical apoptosis - analyzed by flow cytometry (i.e., active caspases 3/7) and western-blot (i.e., cleaved caspase-3 and PARP-1) - is quite low in these conditions, suggesting the participation of other cell death pathways. There is little consensus in the cell death pathways involved in ALS, which is unsurprising given the complexity of the central nervous system and this neurodegenerative disease. Although some changes in the expression of apoptosis-related proteins, such as BCL-2 family proteins, and activation of caspases is present in tissues derived from patients or animal models of ALS [37], no anti-apoptotic agents are of current use or study as an ALS putative therapy. Moreover, apoptosis is considered "immunologically silent," contrasting with the known neuroinflammation of ALS, being one of the main hallmarks of this pathology [38]. Other studies reported necrotic features such as swelling, disrupted plasma membranes, the release of intracellular contents, and neuroinflammation in ALS [38]. These phenotypes could be related to other cell death pathways that present necrosis as an endpoint, such as necroptosis, ferroptosis, or pyroptosis, to name a few. Molecular

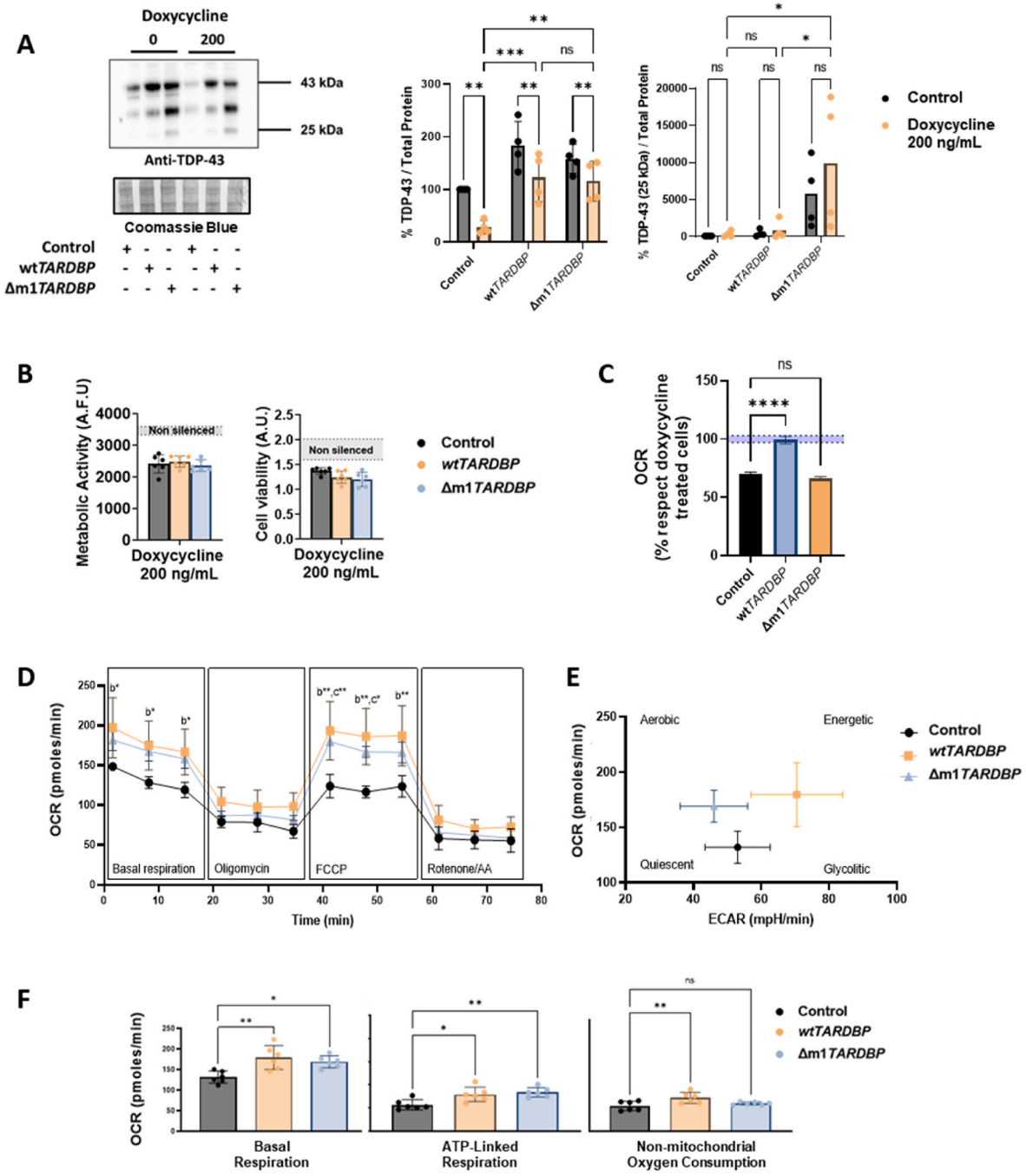

Fig. 4. Transfection of TARDBP and Δm1TARDBP rescues mitochondrial phenotypes impinged by TARDBP loss in pLKO cells. (A) TDP-43 protein levels of pLKO cells un/treated with doxycycline (200 ng/mL) 72h and transfected with GFP, wtTARDBP and Δm1TARDBP plasmids.(B) Metabolic activity (left) and cell viability (right) of pLKO cells treated with doxycycline (200 ng/mL) for 72h and transfected with GFP, wtTARDBP and Δm1TARDBP (C) OCR employing the Resipher apparatus of pLKO cells treated with doxycycline (200 ng/mL) 72h and transfected with GFP, wtTARDBP and Δm1 TARDBP plasmids. (D) OCR employing the Seahorse™ apparatus, normalized for cell number, of pLKO cells treated with doxycycline (200 ng/mL) 72h and transfected with GFP, wtTARDBP and Δm1 TARDBP plasmids, as measured in Fig. 2. (E) Energy Map of pLKO cells treated with doxycycline (200 ng/mL) 72h and transfected with GFP, wtTARDBP and Δm1TARDBP plasmids. (F) pLKO treated with doxycycline 200 ng/mL and transfected with GFP, wtTARDBP and Δm1TARDBP plasmids differences in OCR during basal respiration, ATP-linked respiration, and non-mitochondrial oxygen consumption, respectively. In (A) differences are analyzed by two-way ANOVA and Tukey's-corrected multiple comparisons test. In (B) and (C) shadows of profiles indicate a 95 % confidence interval for measured data. In (C), (D), and (F) differences were determined by one-way ANOVA and Sidak's-corrected multiple comparisons tests. Western-blot analyses (A) were normalized to protein content, measured by densitometric analysis of total protein load by Coomassie Blue staining. *, **, *** and **** indicate, respectively $p < 0.05$, $p < 0.01$, $p < 0.001$, and $p < 0.0001$. (For interpretation of the references to color in this figure legend, the reader is referred to the Web version of this article.)

hallmarks of these death pathways include RIPK-1 and MLKL (necroptosis); caspase 1 and inflammasome components (pyroptosis); ROS overproduction and glutathione peroxidase 4 (GPX4) dysfunction (ferroptosis). These pathways have been related to ALS neuron demise, most of them only in animal and cellular models of ALS [38]. A recent report indicates that ALS patients show depleted GPX4 in post-mortem spinal cords of both sporadic and familial ALS patients. Ongoing clinical trials by ferroptosis and necroptosis inhibitors [39,40] support that these cell

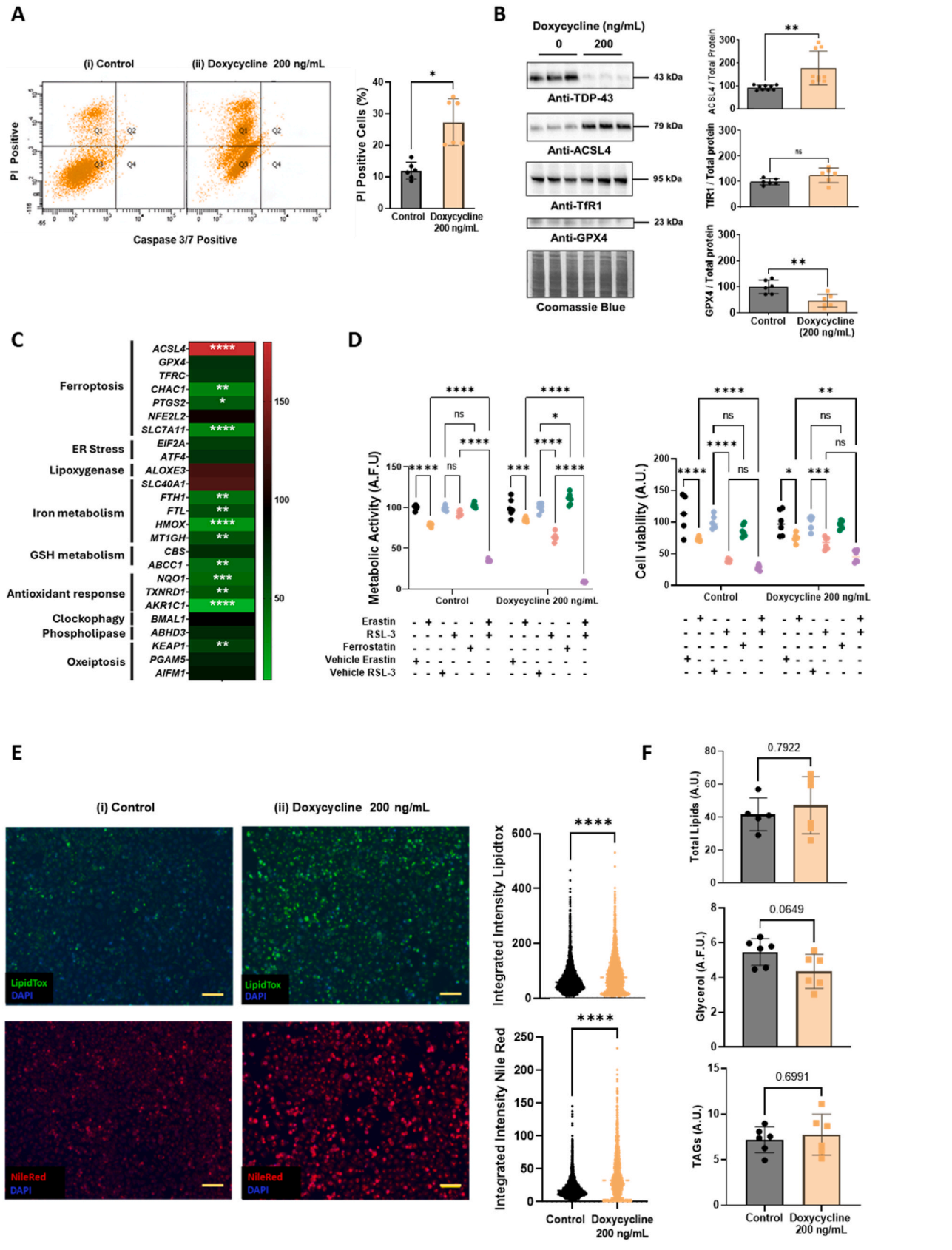

(caption on next page)

Fig. 5. Loss of TARDBP induces an apoptosis-independent cell death in HeLa cells and a build-up of LD. (A) Representative scatter plot of flow cytometry analysis of pLKO cells un/treated with doxycycline (200 ng/mL) 72h (left) and cell death accounting for PI positive cells (right). (B) Representative western-blot (left panels) and densitometry (right panels) of ferroptosis biomarkers after 72h doxycycline (200 ng/mL) treatment in pLKO cells. (C) mRNA levels of selected components of ferroptosis and oxeiptosis after 72h doxycycline (200 ng/mL) treatment in pLKO cells. (D) Metabolic activity (left) and cell viability (right) of pLKO cells after doxycycline (200 ng/mL) addition for 72h and treated with ferroptosis inducers Erastin (50 μM) and RSL-3 (10 μM) or inhibitor Ferrostatin (10 μM) for 24h (E) Fluorescence imaging of pLKO cells un/treated with doxycycline (200 ng/mL) 72h. Nuclei (in blue) were stained with NacBlue™. Neutral lipids (in green) were stained with LipidTOX™. Lipid droplets (in red) were stained with Nile Red. The right panels show the integrated intensity of LipidTOX™ and Nile Red. Scale bar: 20 μm. (F) Total lipids, glycerol and TAG's content analysis in pLKO cells un/treated with doxycycline (200 ng/mL) for 72h. In (A), (B), (E) and (F) differences were analyzed by Student's t-test. In (C) and (D) differences were analyzed by two-way ANOVA and Sidak's-corrected multiple comparisons test. All western-blot analyses were normalized to protein content, measured by densitometric analysis of total protein load by Coomassie Blue staining. *, **, *** and **** indicate $p < 0.05$, $p < 0.01$, $p < 0.001$ and 0.0001. (For interpretation of the references to color in this figure legend, the reader is referred to the Web version of this article.)

death pathways may be relevant in ALS neurodegeneration, and our data support a potential role of *TARDBP* as a novel regulator of specific ferroptosis modules. In addition, an interplay between different death pathways could be possible as shown by beneficial effects of different cell death inhibitors in the same ALS models [37].

In line with this interplay, silencing of *TARDBP* led to higher levels of ACSL4 and a lower amount of GPX4 mRNA, known ferroptosis biomarkers [26]. Ferroptosis could be an interesting candidate for cell death mechanism as it is related to many pathophysiological hallmarks of ALS, such as impaired metabolism and oxidative stress (e.g., lipid peroxidation and accumulation of ROS), but also neuroinflammation (e.g., DAMPs/PAMPs releasing and cytokine production) [38,41]. However, in our case, though classical ferroptosis inducers (RSL-3 and Erastin) induced a loss of viability, it was not additive to *TARDBP* loss. Indeed, *TARDBP* loss decreased the expression of several genes involved in iron metabolism, which may be an adaptive response of pLKO cells to increased oxidative stress. Experimentally induced iron overload in the nervous system increases ACSL4 and decreases SLC7A11 mRNA levels, associated with lipid cacostasis [42]. Thus, we hypothesize that increased ACSL4 mRNA and protein levels might be a part of the response towards compromised oxidative metabolism. Nonetheless, *TARDBP*-loss mediated increase in ACSL4 might contribute to buildup of triacylglyceride synthesis, recently related to ALS development [43]. Also, in the cellular context ACSL4 not only promotes intracellular lipogenesis and LD accumulation but also enhances fatty acid oxidation and ATP production by increasing beta-oxidation limiting enzymes [44]. *TARDBP*-loss fueled lipid accumulation might be also related to defective autophagy and to increased needs for membrane synthesis, which would agree with recent data showing the ferroptosis-independent role of ACSL4 in lipophagy [26]. Of note, recent reports show that alterations in endoplasmic reticulum-mitochondria contacts are prominent in other ALS models, such as the SOD1 mutant mice [45,46]. These contact sites are relevant in lipid synthesis [47] and autophagy, suggesting that TARDBP loss could contribute to mitochondrial stress in a multifaceted way, also involving third-party members, such as endoplasmic reticulum. Accounting the fact that *TARDBP* dysfunction leads to accumulation of aberrant mRNA in selected genes, such as ATG4b, a key autophagy regulator [15], we hypothesize that increased ACSL4 could be a compensatory response towards altered mitochondrial metabolism impinged by *TARDBP* loss-of-function, resulting in altered lipid metabolism.

5. Conclusions

The cellular model evaluated demonstrates that basic cellular traits, such as ATP production, VO2, and cell survival are highly intertwined and dependent on *TARDBP* function. A single cell death mechanism explaining loss of viability induced by TDP-43 loss cannot be inferred, with increased oxidative stress and lipid cacostasis being suggested as a side-effect of bioenergetic compensations to overcome *TARDBP* loss.

Funding

This research was funded by the "Instituto de Salud Carlos III" (PI 17–000134, PI 20–0155, PI23/00176, PI20/0098) and the "Diputació de Lleida" (PP10601—PIRS2021) to M.P.O., R.M.S and A.G.; Also from the "Diputació de Lleida" (PP10605—PIRS2021) and the "Generalitat de Catalunya": Agency for Management of University and Research Grants (2021SGR00990) to R.P.; Support was also received in the form of a FUNDELA Grant, "RedELA-Plataforma Investigación" and the "Fundació Miquel Valls" (Jack Van den Hoek donation).; M.C.C. and M.B.P are "University of Lleida" PhD fellows.; A.F.B. is a "Fundació LaCaixa" postdoctoral fellow.; P.T. is a "Margarita Salas" postdoctoral fellow from the Spanish Ministry of Universities funded by European Union-NextGenerationEI funds.; S.R.R. and M.P.M are "FI AGAUR'' PhD fellows from the Department of Research and Universities of the "Generalitat de Catalunya." FEDER funds are acknowledged ("A way to make Europe"). These funding bodies had no roles in the design of the study, collection, analysis, interpretation of data and in writing the manuscript.

CRediT authorship contribution statement

Miriam Ceron-Codorniu: Writing – original draft, Supervision, Investigation, Formal analysis. **Pascual Torres:** Resources, Methodology. **Anna Fernàndez-Bernal:** Supervision, Formal analysis. **Santiago Rico-Rios:** Resources, Investigation. **José CE. Serrano:** Methodology, Investigation, Formal analysis, Data curation. **Maria P. Miralles:** Investigation, Conceptualization. **Maria Beltran:** Resources, Methodology. **Ana Garcera:** Methodology. **Rosa M. Soler:** Visualization, Supervision, Resources. **Reinald Pamplona:** Writing – original draft, Supervision, Project administration, Funding acquisition. **Manuel Portero-Otín:** Writing – review & editing, Writing – original draft, Visualization, Validation, Supervision, Resources, Project administration, Funding acquisition.

Declaration of competing interest

To whom it may be of interest.

On behalf of all the authors, I hereby confirm that the authors of "*Loss of TDP-43 Induces ALS-Related Collapse of Cellular Homeostasis*" have not declared or known conflicts of interest.

And to confirm that I sign the present in Lleida, at June 4th, 2024.

Data availability

Data will be made available on request.

Acknowledgments

We thank Dr Anaïs Panosa, from the IRBLleida Flow Cytometry Core Facility, for her support in flow cytometry and TEM analyses. We thank Professors Josep E Esquerda and Olga Tarabal for their help in image analyses.

Appendix A. Supplementary data

Supplementary data to this article can be found online at https://doi.org/10.1016/j.redox.2024.103301.

References

[1] W. Robberecht, T. Philips, The changing scene of amyotrophic lateral sclerosis, Nat. Rev. Neurosci. 14 (4) (2013) 248–264, https://doi.org/10.1038/nrn3430.

[2] R. Mejzini, L.L. Flynn, I.L. Pitout, S. Fletcher, S.D. Wilton, P.A. Akkari, ALS Genetics, mechanisms, and therapeutics: where are we now? Front. Neurosci. 13 (2019) https://doi.org/10.3389/fnins.2019.01310. Frontiers Media S.A.

[3] T.R. Suk, M.W.C. Rousseaux, The role of TDP-43 mislocalization in amyotrophic lateral sclerosis, Mol. Neurodegener. 15 (1) (2020), https://doi.org/10.1186/s13024-020-00397-1. BioMed Central Ltd.

[4] J. Janssens, C. Van Broeckhoven, Pathological mechanisms underlying TDP-43 driven neurodegeneration in FTLD-ALS spectrum disorders, Hum. Mol. Genet. 22 (R1) (2013), https://doi.org/10.1093/hmg/ddt349.

[5] P. Smethurst, J. Newcombe, C. Troakes, R. Simone, Y.R. Chen, R. Patani, K. Sidle, In vitro prion-like behaviour of TDP-43 in ALS, Neurobiol. Dis. 96 (2016) 236–247, https://doi.org/10.1016/j.nbd.2016.08.007.

[6] T.F. Gendron, R. Rademakers, L. Petrucelli, TARDBP mutation analysis in TDP-43 proteinopathies and deciphering the toxicity of mutant TDP-43, J. Alzheim. Dis. 33 (SUPPL. 1) (2013), https://doi.org/10.3233/JAD-2012-129036. IOS Press.

[7] P. Torres, P. Andrés-Benito, A. Fernàndez-Bernal, M. Ricart, V. Ayala, R. Pamplona, I. Ferrer, M. Portero-Otin, Selected cryptic exons accumulate in hippocampal cell nuclei in Alzheimer's disease with and without associated TDP-43 proteinopathy, Brain 143 (3) (2020) E20, https://doi.org/10.1093/brain/awaa013. Oxford University Press.

[8] J.P. Ling, O. Pletnikova, J.C. Troncoso, P.C. Wong, TDP-43 repression of nonconserved cryptic exons is compromised in ALS-FTD, Science 349 (6248) (2015) 650–655, https://doi.org/10.1126/science.aab0983.

[9] A. Prasad, V. Bharathi, V. Sivalingam, A. Girdhar, B.K. Patel, Molecular mechanisms of TDP-43 misfolding and pathology in amyotrophic lateral sclerosis, Front. Mol. Neurosci. 12 (2019), https://doi.org/10.3389/fnmol.2019.00025. Frontiers Media S.A.

[10] M.L. Floare, S.P. Allen, Why TDP-43? Why not? Mechanisms of metabolic dysfunction in amyotrophic lateral sclerosis, Neuroscience Insights 15 (2020), https://doi.org/10.1177/2633105520957302. SAGE Publications Ltd.

[11] J. Gao, L. Wang, T. Yan, G. Perry, X. Wang, TDP-43 proteinopathy and mitochondrial abnormalities in neurodegeneration, Mol. Cell. Neurosci. 100 (2019), https://doi.org/10.1016/j.mcn.2019.103396. Academic Press Inc.

[12] P. Wang, J. Deng, J. Dong, J. Liu, E.H. Bigio, M. Mesulam, T. Wang, L. Sun, L. Wang, A.Y.L. Lee, W.A. McGee, X. Chen, K. Fushimi, L. Zhu, J.Y. Wu, TDP-43 induces mitochondrial damage and activates the mitochondrial unfolded protein response, PLoS Genet. 15 (5) (2019), https://doi.org/10.1371/journal.pgen.1007947.

[13] D. Wiederschain, S. Wee, L. Chen, A. Loo, G. Yang, A. Huang, Y. Chen, G. Caponigro, Y.M. Yao, C. Lengauer, W.R. Sellers, J.D. Benson, Single-vector inducible lentiviral RNAi system for oncology target validation, Cell Cycle 8 (3) (2009) 498–504, https://doi.org/10.4161/cc.8.3.7701.

[14] M. Wiznerowicz, D. Trono, Conditional suppression of cellular genes: lentivirus vector-mediated drug-inducible RNA interference, J. Virol. 77 (16) (2003) 8957–8961, https://doi.org/10.1128/JVI.77.16.8957-8961.2003.

[15] P. Torres, O. Ramírez-Núñez, R. Romero-Guevara, G. Barés, A.B. Granado-Serrano, V. Ayala, J. Boada, L. Fontdevila, M. Povedano, D. Sanchís, R. Pamplona, I. Ferrer, M. Portero-Otín, Cryptic exon splicing function of TARDBP interacts with autophagy in nervous tissue, Autophagy 14 (8) (2018) 1398–1403, https://doi.org/10.1080/15548627.2018.1474311.

[16] Z.W. Du, H. Chen, H. Liu, J. Lu, K. Qian, C.T.L. Huang, X. Zhong, F. Fan, S. C. Zhang, Generation and expansion of highly pure motor neuron progenitors from human pluripotent stem cells, Nat. Commun. 6 (2015), https://doi.org/10.1038/ncomms7626.

[17] O. Ramírez-Nuñez, M. Jové, P. Torres, J. Sol, L. Fontdevila, R. Romero-Guevara, P. Andrés-Benito, V. Ayala, C. Rossi, J. Boada, M. Povedano, I. Ferrer, R. Pamplona, M. Portero-Otin, Nuclear lipidome is altered in amyotrophic lateral sclerosis: a pilot study, J. Neurochem. 158 (2) (2021) 482–499, https://doi.org/10.1111/jnc.15373.

[18] M. Feoktistova, P. Geserick, M. Leverkus, Crystal violet assay for determining viability of cultured cells, Cold Spring Harb. Protoc. 2016 (4) (2016), https://doi.org/10.1101/pdb.prot087379 pdb.prot087379.

[19] D.R. Stirling, A.E. Carpenter, B.A. Cimini, CellProfiler Analyst 3.0: accessible data exploration and machine learning for image analysis, Bioinformatics 37 (21) (2021) 3992–3994.

[20] S. Hernández, S. Salvany, A. Casanovas, L. Piedrafita, M.C. Soto-Bernardini, O. Tarabal, A. Blasco, S. Gras, A. Gatius, M.H. Schwab, J. Calderó, J.E. Esquerda, Persistent NRG1 type III overexpression in spinal motor neurons has No therapeutic effect on ALS-related pathology in SOD1G93A mice, Neurotherapeutics 20 (6) (2023) 1820–1834, https://doi.org/10.1007/s13311-023-01424-x.

[21] J. Lam, P. Katti, M. Biete, M. Mungai, S. Ashshareef, K. Neikirk, E.G. Lopez, Z. Vue, T.A. Christensen, H.K. Beasley, T.A. Rodman, S.A. Murray, J.L. Salisbury, B. Glancy, J. Shao, R.O. Pereira, E.D. Abel, A. Hintonjr, A universal approach to analyzing transmission electron microscopy with imagej, Cells 10 (9) (2021), https://doi.org/10.3390/cells10092177.

[22] E. Ahler, W.J. Sullivan, A. Cass, D. Braas, A.G. York, S.J. Bensinger, T.G. Graeber, H.R. Christofk, Doxycycline alters metabolism and proliferation of human cell lines, PLoS One 8 (5) (2013), https://doi.org/10.1371/journal.pone.0064561.

[23] W. Wang, L. Wang, J. Lu, S.L. Siedlak, H. Fujioka, J. Liang, S. Jiang, X. Ma, Z. Jiang, E.L. Da Rocha, M. Sheng, H. Choi, P.H. Lerou, H. Li, X. Wang, The inhibition of TDP-43 mitochondrial localization blocks its neuronal toxicity, Nat. Med. 22 (8) (2016) 869–878, https://doi.org/10.1038/nm.4130.

[24] K. Newton, G. Manning, Necroptosis and inflammation, Annu. Rev. Biochem. 85 (2016) 743–763, https://doi.org/10.1146/annurev-biochem-060815-014830.

[25] Z. Su, Z. Yang, L. Xie, J.P. Dewitt, Y. Chen, Cancer therapy in the necroptosis era, Cell Death Differ. 23 (5) (2016) 748–756, https://doi.org/10.1038/cdd.2016.8. Nature Publishing Group.

[26] X. Chen, P.B. Comish, D. Tang, R. Kang, Characteristics and biomarkers of ferroptosis, Front. Cell Dev. Biol. 9 (2021), https://doi.org/10.3389/fcell.2021.637162. Frontiers Media S.A.

[27] V. Ayala, A.B. Granado-Serrano, D. Cacabelos, A. Naudí, E.V. Ilieva, J. Boada, V. Caraballo-Miralles, J. Lladó, I. Ferrer, R. Pamplona, M. Portero-Otin, Cell stress induces TDP-43 pathological changes associated with ERK1/2 dysfunction: implications in ALS, Acta Neuropathol. 122 (3) (2011) 259–270, https://doi.org/10.1007/s00401-011-0850-y.

[28] A.N. Coyne, B.L. Zaepfel, D.C. Zarnescu, Failure to deliver and translate—new insights into RNA dysregulation in ALS, Front. Cell. Neurosci. 11 (2017), https://doi.org/10.3389/fncel.2017.00243. Frontiers Media S.A.

[29] N.R. Stallings, K. Puttaparthi, K.J. Dowling, C.M. Luther, D.K. Burns, K. Davis, J. L. Elliott, TDP-43, an ALS linked protein, regulates fat deposition and glucose homeostasis, PLoS One 8 (8) (2013), https://doi.org/10.1371/journal.pone.0071793.

[30] T.W. Tefera, F.J. Steyn, S.T. Ngo, K. Borges, CNS glucose metabolism in Amyotrophic Lateral Sclerosis: a therapeutic target? Cell Biosci. 11 (Issue 1) (2021) https://doi.org/10.1186/s13578-020-00511-2. BioMed Central Ltd.

[31] T. Vandoorne, K. De Bock, L. Van Den Bosch, Energy metabolism in ALS: an underappreciated opportunity? Acta Neuropathol. 135 (4) (2018) 489–509, https://doi.org/10.1007/s00401-018-1835-x. Springer Verlag.

[32] C. Garza-Lombó, A. Pappa, M.I. Panayiotidis, R. Franco, Redox homeostasis, oxidative stress and mitophagy, Mitochondrion 51 (2020) 105–117, https://doi.org/10.1016/j.mito.2020.01.002. Elsevier B.V.

[33] B.A. Berning, A.K. Walker, The pathobiology of TDP-43 C-terminal fragments in ALS and FTLD, Front. Neurosci. 13 (Issue APR) (2019), https://doi.org/10.3389/fnins.2019.00335. Frontiers Media S.A.

[34] D. Chhangani, A. Martín-Peñ, D.E. Rincon-Limas, iScience Molecular, functional, and pathological aspects of TDP-43 fragmentation, iScience 24 (2021) 102459, https://doi.org/10.1016/j.isci.

[35] L.M. Igaz, L.K. Kwong, A. Chen-Plotkin, M.J. Winton, T.L. Unger, Y. Xu, M. Neumann, J.Q. Trojanowski, V.M.Y. Lee, Expression of TDP-43 C-terminal fragments in vitro recapitulates pathological features of TDP-43 proteinopathies, J. Biol. Chem. 284 (13) (2009) 8516–8524, https://doi.org/10.1074/jbc.M809462200.

[36] P.E.A. Ash, Y.J. Zhang, C.M. Roberts, T. Saldi, H. Hutter, E. Buratti, L. Petrucelli, C. D. Link, Neurotoxic effects of TDP-43 overexpression in C. elegans, Hum. Mol. Genet. 19 (16) (2010) 3206–3218, https://doi.org/10.1093/hmg/ddq230.

[37] D. Moujalled, A. Strasser, J.R. Liddell, Molecular mechanisms of cell death in neurological diseases, Cell Death Differ. 28 (7) (2021) 2029–2044, https://doi.org/10.1038/s41418-021-00814-y. Springer Nature.

[38] D.V. Neel, H. Basu, G. Gunner, I.M. Chiu, Catching a killer: mechanisms of programmed cell death and immune activation in Amyotrophic Lateral Sclerosis, Immunol. Rev. 311 (1) (2022) 130–150, https://doi.org/10.1111/imr.13083. John Wiley and Sons Inc.

[39] C. Moreau, V. Danel, J.C. Devedjian, G. Grolez, K. Timmerman, C. Laloux, M. Petrault, F. Gouel, A. Jonneaux, M. Dutheil, C. Lachaud, R. Lopes, G. Kuchcinski, F. Auger, M. Kyheng, A. Duhamel, T. Pérez, P.F. Pradat, H. Blasco, D. Devos, Could conservative iron chelation lead to neuroprotection in amyotrophic lateral sclerosis? Antioxidants Redox Signal. 29 (8) (2018) 742–748, https://doi.org/10.1089/ars.2017.7493.

[40] S. Nikseresht, J.B.W. Hilton, K. Kysenius, J.R. Liddell, P.J. Crouch, Copper-ATSM as a treatment for ALS: support from mutant SOD1 models and beyond, Life 10 (11) (2020) 1–14, https://doi.org/10.3390/life10110271. MDPI AG.

[41] Y. Ma, F. Han, J. Min, W. Lin, Energy metabolism as a regulator of ferroptosis, Cell Cycle 19 (22) (2020) 2960–2962, https://doi.org/10.1080/15384101.2020.1838781.

[42] A. Maniscalchi, O.N. Benzi Juncos, M.A. Conde, M.I. Funk, M.E. Fermento, M. M. Facchinetti, A.C. Curino, R.M. Uranga, N.P. Alza, G.A. Salvador, New insights on neurodegeneration triggered by iron accumulation: intersections with neutral lipid metabolism, ferroptosis, and motor impairment, Redox Biol. 71 (2024), https://doi.org/10.1016/j.redox.2024.103074.

[43] J.C. Dodge, E.H. Jensen, J. Yu, S. Pablo Sardi, A.R. Bialas, T.V. Taksir, D.S. Bangari, L.S. Shihabuddin, Neutral lipid cacostasis contributes to disease pathogenesis in

amyotrophic lateral sclerosis, J. Neurosci. 40 (47) (2020) 9137–9147, https://doi.org/10.1523/JNEUROSCI.1388-20.2020.

[44] J. Lin, P. Zhang, W. Liu, G. Liu, J. Zhang, M. Yan, Y. Duan, N. Yang, A positive feedback loop between ZEB2 and ACSL4 regulates lipid metabolism to promote breast cancer metastasis. https://doi.org/10.7554/eLife.87510.3, 2023.

[45] Larrea, D., Tamucci, K. A., Kabra, K., Velasco, K. R., Yun, T. D., Pera, M., Montesinos, J., Agrawal, R. R., Smerdon, J. W., Lowry, E. R., Stepanova, A., Yoval-Sanchez, B., Galkin, A., Wichterle, H., & Area-Gomez, E. (n.d.). Altered MAM function shifts mitochondrial metabolism in SOD1-mutant models of ALS. https://doi.org/10.1101/2022.09.22.508778.

[46] S. Salvany, A. Casanovas, L. Piedrafita, S. Gras, J. Calderó, J.E. Esquerda, Accumulation of misfolded SOD1 outlines distinct patterns of motor neuron pathology and death during disease progression in a SOD1G93A mouse model of amyotrophic lateral sclerosis, Brain Pathol. 32 (6) (2022), https://doi.org/10.1111/bpa.13078.

[47] A.F. Bernal, N. Mota, R. Pamplona, E. Area-Gomez, M. Portero-Otin, Hakuna MAM-Tata: investigating the role of mitochondrial-associated membranes in ALS, Biochim. Biophys. Acta (BBA) - Mol. Basis Dis. 1869 (6) (2023), https://doi.org/10.1016/j.bbadis.2023.166716. Elsevier B.V.